

Molecular gas and dust properties in $z > 7$ quasar hosts

Francesco Salvestrini^{1,2}, Chiara Feruglio^{1,2}, Roberta Tripodi³, Fabio Fontanot^{1,2}, Manuela Bischetti^{4,1,2}, Gabriella De Lucia^{1,2}, Fabrizio Fiore^{1,2}, Michaela Hirschmann^{5,1}, Umberto Maio^{1,2}, Enrico Piconcelli⁶, Ivano Saccheo^{7,6}, Alessia Tortosa⁶, Rosa Valiante^{6,8}, Lizhi Xie^{9,1}, and Luca Zappacosta⁶

¹ INAF - Osservatorio Astronomico di Trieste, Via G. Tiepolo 11, I-34143 Trieste, Italy

² IFPU - Institute for Fundamental Physics of the Universe, via Beirut 2, I-34151 Trieste, Italy

³ University of Ljubljana, Department of Mathematics and Physics, Jadranska ulica 19, SI-1000 Ljubljana, Slovenia

⁴ Dipartimento di Fisica, Università di Trieste, Sezione di Astronomia, Via G.B. Tiepolo 11, I-34131 Trieste, Italy

⁵ Institute for Physics, Laboratory for Galaxy Evolution and Spectral Modelling, Ecole Polytechnique Federale de Lausanne, Observatoire de Sauvigny, Chemin Pegasi 51, CH-1290 Versoix, Switzerland

⁶ INAF-Osservatorio Astronomico di Roma, Via Frascati 33, I-00040 Monte Porzio Catone, Italy

⁷ Dipartimento di Matematica e Fisica, Università Roma Tre, Via della Vasca Navale 84, I-00146 Roma, Italy

⁸ INFN-Sezione Roma1, Dipartimento di Fisica, Università di Roma La Sapienza, Piazzale Aldo Moro 2, I-00185 Roma, Italy

⁹ Tianjin Normal University, Binshuixidao 393, Xiqing, 300387, Tianjin, People's Republic of China

ABSTRACT

Observational campaigns hunting the elusive reservoirs of cold gas in the host galaxies of quasars at the Epoch of Reionization (EoR) are crucial to study the formation and evolution of the first massive systems at early epochs. We present new Northern Extended Millimetre Array (NOEMA) observations tracing CO(6–5), CO(7–6) emission lines, and the underlying continuum in five of the eight quasars at redshift $z > 7$ known to date, thus completing the survey of the cold molecular gas reservoir in the host galaxies of the first quasars. Combining NOEMA observations with archival Atacama Large Millimeter Array (ALMA) data available, we model the far-infrared spectral energy distribution with a modified blackbody to measure dust properties and star formation rates. We use CO and [CII] lines to derive molecular gas masses, which we compare with results from semi-analytical models and observations of galaxies at different epochs. No statistically significant detection of CO emission lines was reported for the five quasars in this sample, resulting in a relatively low amount of cold molecular gas in the host when compared with galaxies at later epochs. Nonetheless, gas-to-dust ratios are consistent with the local value, suggesting that the scaling relation between dust and cold gas holds up to $z > 7$. Quasars at the EoR show star formation efficiencies which are among the highest observed so far, but comparable with that observed in luminous quasar at Cosmic Noon and that predicted for the brightest ($L_{bol} > 3 \times 10^{46}$ erg s⁻¹) quasar objects drawn from the semi-analytical model GAEA. Quasar host galaxies at the EoR are undergoing an intense phase of star formation, which suggests a strong coupling between the luminous phase of the quasar and the rapid growth of the host.

Key words. Quasars: emission lines - Galaxies: ISM - Galaxies: evolution - Galaxies: high-redshift

1. Introduction

The relevant role of quasars in re-ionizing the Universe at $z > 6$ has been known for many years (Gunn & Peterson 1965). However, our understanding has advanced considerably over the past couple of decades, paralleling the growth in the number of known quasars, which now includes approximately 300 quasars identified at the Epoch of Reionization (EoR) (Fan et al. 2023). This has been achieved thanks to the combination of near-infrared photometric surveys and spectroscopic follow-up observations, which have proven to be a reliable tool to discover the quasar population at high-redshift ($z > 5$; e.g., Bañados et al. 2016; Shen et al. 2019).

Luminous quasars at the EoR are also crucial probes for testing the co-evolution between supermassive black holes (SMBHs) and their host galaxy. In this regard, modern interferometric facilities have been essential to confirm the redshift of the objects, to constrain the star formation activity, and the properties of the cold phase of the interstellar medium (ISM) of their host-galaxy (e.g., Riechers et al. 2006, 2007, 2009; Wang et al. 2007, 2010). Indeed, far-infrared/sub-mm observations have revealed the presence of highly star-forming host-galaxies, with

star formation rates (SFR) up to 1000-3000 M_{\odot} yr⁻¹, and copious amount of dust ($M_{dust} > 10^8 M_{\odot}$; Maiolino et al. 2005; Wang et al. 2013; Feruglio et al. 2018; Pensabene et al. 2022; Venemans et al. 2017b, 2020). These massive quasar hosts are crucial for benchmarking gas and dust content and star formation efficiencies (SFE) during the mid-point and terminal stages of the Reionization epoch, but observations are still limited to a few tens of quasar hosts at these epochs. Furthermore, the scaling relation between gas and dust is not clear yet, and the methods that are currently adopted to derive molecular gas masses can be improved with more data available. Given its brightness, the 158 μ m emission line of the singly ionized carbon atom ([CII] hereafter) is the most used tracer of the ISM at $z > 4$. While the [CII] emission is undoubtedly useful and powerful for dynamical studies (e.g., Wang et al. 2013; Decarli et al. 2017; Venemans et al. 2019, 2020; Neeleman et al. 2021; Wang et al. 2024), it may not effectively trace the dense and cold components of the molecular gas, nor the star-forming regions (e.g., Pineda et al. 2013; Herrera-Camus et al. 2018; Neeleman et al. 2019; Bischetti et al. 2024; Izumi et al. 2024). On the other hand, the rotational excited transitions of the carbon monoxide (CO) are much more reliable probes of the dense cold H_2 and are

Table 1: NOEMA observations

Name	Ra,Dec J2000	z [C II]	Freq. [GHz]	Beam [arcsec ²]	R.m.s. [μ Jy/beam]	S_ν [μ Jy]	Size [arcsec ²]
J0313-1806	03:13:43.84, -18 : 06 : 36.40	7.6423	USB 92.568	13.1×3.7	48.5	$< 100.5^{(a)}$	0.71×0.55
			LSB 78.756	16.4×4.3	46.3	–	
			219.911	0.62×0.44	19	0.50 ± 0.05	
J1243+0100	12:43:53.93, 01:00:38.50	7.0749	USB 100.310	5.8×2.3	16.1	119.0 ± 16.1	0.78×0.72
			LSB 86.756	6.3×2.8	13.0	49.8 ± 12.5	
			235.364	0.62×0.50	19	2.07 ± 0.09	
J0038-1527	00:38:36.10, -15 : 27 : 23.60	7.034	USB 100.821	6.2×3.8	22.3	$< 44.4^{(a)}$	1.9×1.2
			LSB 87.256	7.3×4.4	19.8	–	
			236.562	0.62×0.55	37	1.8 ± 0.7	
J2356+0017	23:56:46.33, 00:17:47.30	7.01	USB 101.373	4.6×3.5	15.8	$94.0 \pm$	
			LSB 87.756	5.4×4.1	13.4	< 40.2	
			237.852	0.56×0.40	35	1.04 ± 0.10	
J0252-0503	02:52:16.64, -05 : 03 : 31.80	7.0006	USB 101.491	5.6×4.2	19.0	123.4 ± 17.8	0.72×0.55
			LSB 87.756	6.6×4.9	15.6	76.9 ± 14.9	
			237.852	0.56×0.40	35	1.04 ± 0.10	

Notes. NOEMA fluxes are derived from a fit of the visibilities with a point source model. ALMA fluxes are the integrated emission of best-fit 2D Gaussian function model of the cleaned continuum map. Upper limits are at the 3σ significance level. R.m.s. is estimated using a channel width of 20 MHz. ^(a) upper limits are computed for the merged USB+LSB continuum data.

pivotal to investigate the star formation process (Kaasinen et al. 2024). Despite being fainter than [C II], CO lines have been successfully revealed in massive quasar hosts at $z \sim 6$ (e.g., Wang et al. 2013; Decarli et al. 2022), but currently remain poorly sampled at the highest redshifts ($z > 7$) of quasars, with only one confirmed individual detection (Feruglio et al. 2023) and possible detection suggested by stacking of multiple lines (Venemans et al. 2017b; Novak et al. 2019), at $z \sim 7.1 - 7.5$.

In this work, we present new observations targeting CO(6-5) and (7-6) emission lines and the underlying continuum in five quasars at $z > 7$, obtained with the Northern Extended Millimeter Array (NOEMA), thus providing a complete census of the molecular gas in the population of $z > 7$ quasars known to date (Fan et al. 2023). We also investigate the star formation activity and dust properties for the five quasars by modeling the far-infrared spectral energy distribution (SED) using NOEMA and archival observations of the Atacama Large Millimeter/Submillimeter Array (ALMA). Based on these measurements, we study the growth of host galaxies and the implications on the co-evolution with the SMBH in the reionization era. This paper is organized as follows. Section 2 describes the observations and data reduction. Section 3 describes the procedures adopted to model the far-infrared (far-IR) SED, to measure the dust and cold molecular gas content, including a new calibration using the [C II] luminosity. In section 4, we discuss the results and their implication on the co-evolution of the host galaxy of quasars at the EoR by comparing them with objects at lower redshift and the results from semi-analytical models. We summarize the paper in section 5.

Throughout the paper, we adopt a standard flat Λ cold dark matter cosmology with the matter density parameter $\Omega_M = 0.30$, the dark energy density parameter $\Omega_\Lambda = 0.70$, and the Hubble constant $H_0 = 70 \text{ km s}^{-1}$.

2. Sample and Observations

We focus on the quasars with $z \geq 7$, which are eight in total according to (Fan et al. 2023), aiming to obtain a complete census of the molecular gas content in these objects. The five quasars

for which we acquired new NOEMA observations under project S23CX are listed in Table 1, while the entire list of $z > 7$ quasars with their names and identifications are reported in Table 2.

Regarding project S23CS, receivers were tuned to detect the CO(6-5) and CO(7-6) and the underlying continuum in the Lower and Upper Side Band (LSB, USB), respectively. We calibrated the visibilities using the CLIC pipeline of the GILDAS software¹. Imaging was performed with MAPPING in GILDAS, using a natural weighting scheme for visibilities, with a detection threshold equal to the noise of the pre-imaging visibilities. The observation targeting quasar J0313 was executed in bad weather conditions, so it did not reach the requested sensitivity to detect either continuum emission or CO lines in both LSB and USB. Given the low declination of J0038 (coordinates are listed in Table 1), the observation of this target was limited by shadowing, which reduced the total observing time on-source, hence the final sensitivity. In these two cases, we merged LSB and USB to increase the signal-to-noise ratio, and we used the merged cube to extract an upper limit on the continuum emission. Continuum-subtracted cubes were binned to spectral resolutions of 20 MHz, corresponding to $\sim 60 \text{ km s}^{-1}$, to optimize the sensitivity.

To extend the sampling of the far-infrared emission of the quasar host galaxies, we collected archival ALMA observations for four of the five quasars², that covers sky frequencies $\sim 220 - 240 \text{ GHz}$, where the [C II] emission line falls. ALMA-calibrated visibilities of observations covering [C II] and the underlying continuum were retrieved from the science archive (see Acknowledgements for the list of ALMA project IDs). The imaging was performed through the Common Astronomy Software Applications (CASA; McMullin et al. 2007), version 6.5.5-21. We run tclean procedures using natural weighting, a 3σ cleaning threshold, and a channel width of 20 MHz. Continuum-subtracted cubes and continuum maps were created using the *imfit* procedure in CASA, fitting a constant function to all line-free channels.

¹ www.iram.fr/IRAMFR/GILDAS

² Project IDs of the dataset analyzed are listed in the Acknowledgements. J2356 observation with project ID 2023.1.00443.S is still in a proprietary period at the moment of this analysis

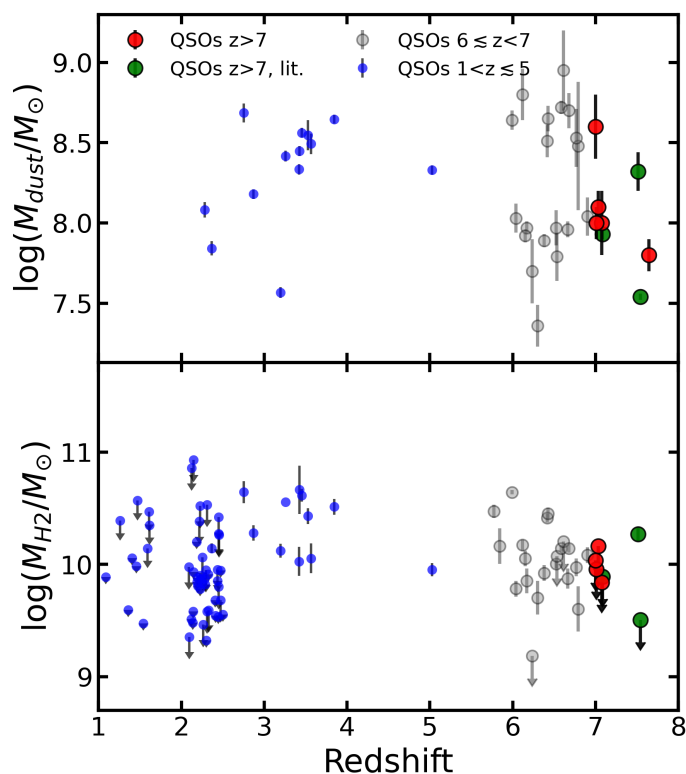


Fig. 1: Dust mass and Molecular gas mass versus redshift. *Upper panel:* M_d vs redshift. Red circles are the $z > 7$ quasars presented in this work. Green circles are for J1120 from Venemans et al. (2017b), J1007 from Feruglio et al. (2023) and J1342 from Novak et al. (2019). Grey circles are the $5 < z < 7$ quasars from Venemans et al. (2017c); Izumi et al. (2021); Decarli et al. (2022); Tripodi et al. (2024a), while blue dots are for quasars at intermediate redshift ($1 < z < 5$) from (Bischetti et al. 2021, and Salvestrini et al., in prep.). *Lower panel:* M_{H_2} vs redshift. Data are color-coded as in the upper panel. In this plot, we also included the quasars at intermediate redshift ($1 < z < 5$) from Bertola et al. (2024).

The synthesized beams, root-mean-square (rms) noise levels, and representative frequencies of the continuum maps are reported in Table 1. Continuum maps of ALMA and NOEMA observations are shown in Fig. B.1.

3. Results

3.1. Dust properties and star formation rate

The continuum maps of the five targets are presented in Fig. B.1. We measured continuum flux densities of NOEMA maps with a fit of the visibilities with a point source model. The associated error accounts for both the statistical uncertainty of the fit and the calibration error ($\lesssim 10\%^3$). For J0252, J1243, and J2356, we also measured the continuum flux by integrating the 2D Gaussian function that fits the cleaned continuum emission map. The two approaches provide flux estimates that are consistent within the uncertainties. In the case of the NOEMA observations, the observing setup did not allow us to spatially resolve the target

³ IRAM NOEMA Data Reduction Cookbook, <https://iram-institute.org/science-portal/noema/documentation/>

extension, all best-fit functions are consistent with a point-like source having a size comparable with the beam (see Table 1). Flux upper limits are estimated at a 3σ significance level using the rms noise and assuming a size equal to the beam size.

As visible in Fig. B.1, ALMA observations of J0038, J0313, J0252, and J1243 spatially resolve the extent of the continuum emission. This allowed us to measure the size of the continuum emitting region in quasar host galaxies by modeling the continuum maps with a 2D Gaussian function. In Table 1, we report the integrated flux and host-galaxy size, which is assumed to be equal to the full-width half maximum (FWHM) of the best-fit 2D Gaussian function.

Using EOS-DUSTFIT⁴, we fitted the cold dust SED of the target galaxies. In EOS-DUSTFIT, following the prescription by Draine & Li (2007, see also Carniani et al. 2019; Tripodi et al. 2024a), the cold dust continuum emission is modeled with a modified black body (MBB) function, assuming an optically thick regime. The MBB model can have up to three free parameters, namely dust temperature (T_d), dust mass (M_d), and the emissivity index (β). However, for the five sources of our sample, the limited number of data prevents modeling the far-infrared SED with three free parameters. In particular, the peak of the SED is not sampled by current data, making it challenging to constrain the dust temperature. Consequently, we adopt a fixed temperature $T_d = 55$ K for all five quasars based on the mean dust temperature in a sample of $10 z > 6$ quasars (Tripodi et al. 2024a). This assumption is further supported by recent literature results on $z > 6$ quasars (e.g., Decarli et al. 2022; Sommovigo et al. 2022; Shao et al. 2022; Witstok et al. 2023; Tripodi et al. 2023) and lower- z quasars with measured T_{dust} (e.g., Bischetti et al. 2021), as it would be expected in the case of compact, and dense star-forming regions (dust sizes of few kpc; e.g., Venemans et al. 2017b; Decarli et al. 2018, 2022; Tripodi et al. 2024a). Their intense star formation still stands even after accounting for the AGN contribution to the dust heating, which can be substantial, especially in the nuclear region (Duras et al. 2017; Di Mascia et al. 2021; Walter et al. 2022; Tsukui et al. 2023).

Combining NOEMA and ALMA detections in the observed-frame ~ 80 -230 GHz range, we estimate the dust emissivity parameter β for two objects in our sample (J0252 and J1243). For the others, we fixed $\beta = 1.6$, i.e., the local value (Beelen et al. 2006; Witstok et al. 2023) and similar to that measured in J0252 and J1243. Since NOEMA observations do not allow us to resolve the source size, we assumed that the size does not vary significantly with frequency in the observed range ~ 80 GHz to ~ 230 GHz. Quasar J2356 only has an unresolved observation at 3 mm (Fig. B.1). Then, we assume a size of 0.75×0.64 arcsec², based on the median value of the FWHM dimensions measured for the four quasars of our sample with ALMA observations.

EOS-Dustfit explores the parameter space for each SED using a Markov chain Monte Carlo algorithm implemented in the *emcee* package (Foreman-Mackey et al. 2013). A uniform distribution for priors is assumed for fitting parameters in the range: $5 < \log(M_d/M_\odot) < 9$ for all the quasars, and $0.5 < \beta < 3.0$ for both J0252 and J1243. We ran 40 chains, with 3000 trials and a burn-in phase of 150 steps for each dataset; we added in quadrature a 10% calibration uncertainty to the continuum flux errors. The upper limits of the continuum emission were included in the

⁴ EOS-DUSTFIT is a publicly available tool for fitting the cold dust SED of galaxies (<https://github.com/roberta96/EOS-Dustfit>), which has been used in this work and in Tripodi et al. (2024a). Details about the modeling can be found on the GitHub page and in Tripodi et al. (2024a).

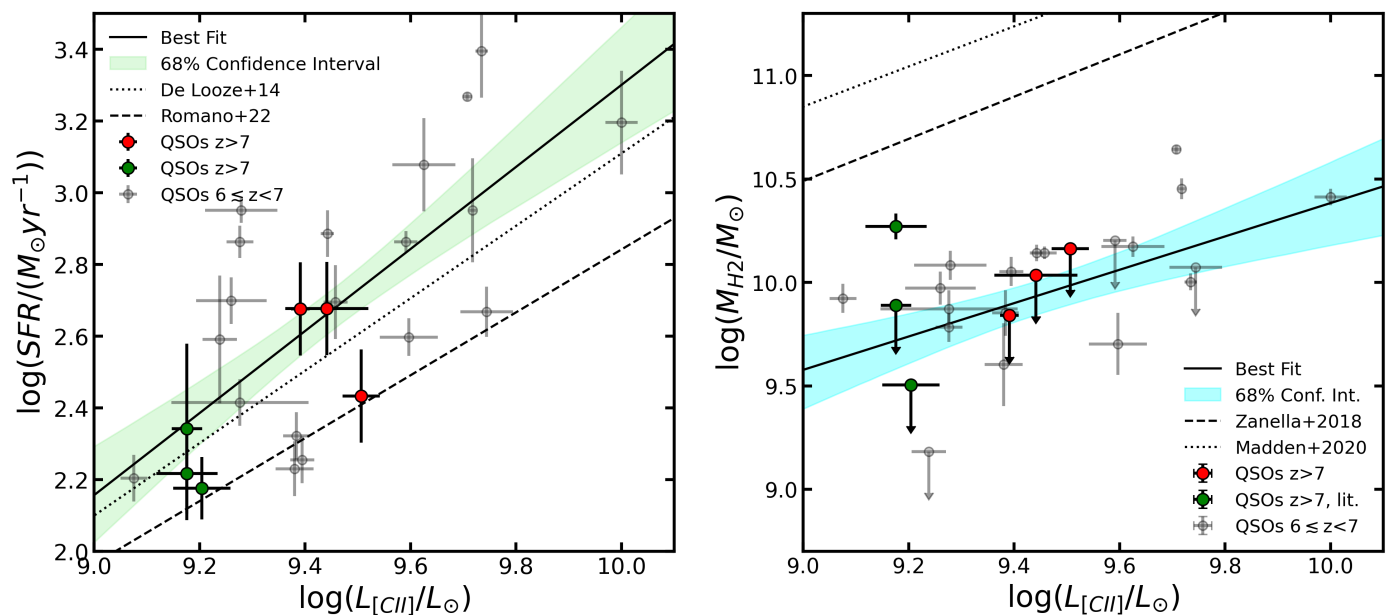


Fig. 2: SFR and molecular gas mass versus [CII] luminosity. *Left panel:* $z > 7$ quasars with $L_{[CII]}$ measurement are J1234, J0038, J0252 (red circles) and J1120, J1342, J1007 (green circle). Grey dots at the quasars at $z \geq 6$ from the literature (see Table C.1) Best-fit relation and the relative 68% confidence interval are represented as the solid black line and green shadowed region, respectively. The best-fit parameters of the relation are: slope $1.15^{+0.28}_{-0.27}$, normalization $-8.16^{+0.06}_{-0.06}$, and intrinsic dispersion $0.07^{+0.03}_{-0.02}$ dex. The dotted line is the relation by De Looze et al. (2014) for low-metallicity dwarf galaxies in the local Universe. The dashed line is best-fit relation by Romano et al. (2022) for galaxies from the ALPINE survey ($4 < z < 6$), including both detections and stacked non-detections. *Right panel:* $z > 7$ quasars with $L_{[CII]}$ measurement and M_{H_2} upper limit are J1234, J0038, J0252 (red circles) and J1342 (green circle), while J1007 has both $L_{[CII]}$ and M_{H_2} measurement. M_{H_2} measurements and upper limit for $z > 5$ from the literature have been homogenized to those presented in this work by assuming a common $\alpha_{CO} = 0.8 M_{\odot} \text{ pc}^{-2} (\text{K km s}^{-1})^{-1}$ and CO SLED. Best-fit relation and the relative 68% confidence interval are represented as the solid black line and gray shadowed region, respectively. The best-fit intrinsic dispersion of the relation is $\delta_{intr} = 0.10^{+0.06}_{-0.03}$ dex. The dashed line is the scaling relation derived by Zanella et al. (2018) for main-sequence and luminous infrared galaxies, up to $z \sim 6$. We also report the scaling relation provided by Madden et al. (2020) for local dwarf galaxies (dotted line).

fit as a 1σ detection with a 2σ error. There is not yet a standard approach for dealing with upper limits in the fitting procedure, one could either treat them as detections with large errors (as we do; see also e.g. Ronconi et al. 2024, Witstok et al. 2022) or change the fitting code properly to ensure that above the upper limit level, the likelihood is zero. We adopt the first method given that it is commonly employed in many fitting routines (e.g., GalaPy, MERCURIUS) and gives us reasonable results. We adopted the 50th percentile of the posterior distribution as the best-fit value, while the errors are calculated considering the 16th and 84th percentiles (corner plots of the posterior distribution of free parameters are shown in Fig. A.2). In the case of the modeling of far-IR SED assuming a fixed β , the uncertainties on M_d are relatively smaller (see below) when compared to the fit where β is left free to vary. This is because of the marginalization over the distribution of β . We have therefore estimated that this underestimates the uncertainty on M_d by ~ 0.05 dex. A similar conclusion can be reached for the assumption of T_d fixed to 55 K. In section 3, we take care of this systematic by including an additional contribution to the error on M_d and L_{FIR} . The results from the SED fitting are reported in Tab. 2, while the best-fit models are shown in Fig. A.1. We measured the far-IR luminosity (L_{FIR}) by integrating the 40-1000 μm emission of the best-fit model produced by Eos-DustFit in the five quasars. SFR is computed with the relation by Kennicutt (1998), $SFR/(M_{\odot} \text{ yr}^{-1}) = 10^{-10} L_{FIR}/L_{\odot}$, assuming a Chabrier initial mass function (IMF) (Chabrier 2003). The same prescription is

commonly assumed in high- z quasars (e.g., Duras et al. 2017; Bischetti et al. 2021; Bertola et al. 2024), and is roughly consistent with the SFR derived assuming a Kroupa (2001) IMF (within 7%). A Chabrier IMF was also adopted for J1007 by Feruglio et al. (2023) and J1342 by Novak et al. (2019), while Venemans et al. (2017b) assumed a Kroupa IMF for J1120.

In two cases we modeled the dust emissivity index, for J1243 the best-fit value derived is fully consistent with the typical value observed in high-redshift quasars (Beelen et al. 2006; Venemans et al. 2017b, 2020; Tripodi et al. 2024a). For J0252, we derived $\beta = 0.93^{+0.20}_{-0.21}$, which is significantly lower (4σ) than β values measured in high- z quasars. A potential reason for the flat far-infrared SED in J0252 could be the presence of contaminant sources within the beam of the NOEMA observation (see Fig. B.1). Indeed, the ALMA continuum map of J0252 (see Fig. B.1) shows a marginally resolved source surrounded by elongated emission features, each detected with $> 2\sigma$ significance level. These emission features may either hide the presence of close companion galaxies or interloper sources. However, the relatively low β value obtained from the fit does not significantly affect the M_d estimate. Assuming $\beta = 1.6$ for J0252, we obtained a M_d fully consistent with the one presented in Table 2.

We tested the consistency of our assumptions (namely, T_d, β) on the results of the SED fitting. Using a higher (lower) dust temperature such as $T_d = 70$ K (40 K) would have led to an average decrease (increase) in M_d by a factor of ~ 1.5 (~ 0.18 dex), while

the value of L_{FIR} would have been higher (lower) by a factor of ~ 2 (~ 0.3 dex). Regarding β , assuming a steeper emissivity index ($\beta = 2$) for the targets with β fixed (namely, J0038, J0313, and J2356) would have resulted in a larger M_{d} (lower L_{FIR}) by a factor of ~ 2 . Conversely, choosing a flatter β ($\beta = 1.2$) corresponds to a mean increase (decrease) of the value of M_{d} (L_{FIR}) of a factor ≤ 1.2 . Eventually, we tested the impact of assuming a different source size: increasing the source area up to a factor 10 provided results consistent within the uncertainties with those listed in Table 2; if the source area was overestimated by a factor of 10 or more, this would have led to M_{d} and L_{FIR} being lower by a factor of ≥ 2 .

The five quasars in our sample show M_{d} in the range $0.4 - 3.2 \times 10^8 M_{\odot}$ (see Fig. 1 and Table 2), consistent with the dust content derived in the population of luminous quasars at the EoR (e.g., Izumi et al. 2021; Witstok et al. 2023; Tripodi et al. 2024a) and at different cosmic epochs (e.g., Duras et al. 2017; Bischetti et al. 2021; Bertola et al. 2024), and star-forming galaxies at lower redshift (e.g., Mancini et al. 2015; Leśniewska & Michałowski 2019; Pozzi et al. 2021; Hygate et al. 2023; Algera et al. 2024). As shown in Fig. 1, comparing quasars at $z > 7$ and sources at later epochs, there is no clear evolution of M_{d} as a function of the redshift. The quasars in our sample have already built large dust masses in a relatively short time (the Hubble time at $z \sim 7$ is ~ 800 Myr), suggesting that in high- z quasar hosts the physical processes that drive the formation of dust grains are very efficient and overtake those processes destroying dust particles (e.g., Popping et al. 2017). We continue the discussion on the dust formation processes in section 4.1.

3.2. Molecular gas mass

For four out of five quasars observed with NOEMA we derive 3σ upper limits on the cold H_2 mass using the rms at the expected frequency of CO(6–5) and (7–6) emission lines. We assume a line width of FWHM = 300 km/s, as expected for $z > 6$ quasars (e.g., Decarli et al. 2022; Feruglio et al. 2023), and a galaxy size equal to the beam of the observations. We adopt a CO spectral line energy distribution (SLED) correction of Kaasinen et al. (2024), that is, $r_{6,1} = 0.92$ for CO(6-5) and $r_{7,1} = 0.65$. Assuming a luminosity to mass conversion factor $\alpha_{\text{co}} = 0.8 M_{\odot}(\text{K km s}^{-1} \text{pc}^2)^{-1}$ (see Bolatto et al. 2013; Carilli & Walter 2013), we then derive an upper limit $M(H_2)$ in the range $\sim 0.9 - 1.5 \times 10^{10} M_{\odot}$ (see Table 2). The same α_{co} and CO SLED correction factor are adopted for the upper limits and estimate of the H_2 masses of J1007, J1120, J1342, for which we collected CO luminosity from the literature and included in Table 2. Of the known quasars at $z \gtrsim 7$, five have only upper limits on their H_2 masses as traced by CO emission lines, with J1007 being the sole source with a statistically significant detection ($> 6\sigma$) of molecular gas mass (Feruglio et al. 2023).

The molecular gas mass and the upper limits for the $z > 7$ quasars (see Table 2 and Fig. 1) are consistent with the mean value measured in the population of $5 < z < 7$ quasars ($\log(M_{H_2}/M_{\odot}) \sim 10 \pm 0.3$; e.g., Venemans et al. 2017c; Decarli et al. 2022; Kaasinen et al. 2024).

To test the consistency of our M_{H_2} upper limits, we compare the CO-derived measurement with that obtained from the [CII]158 μm ([CII], hereafter) luminosity. Indeed, $L_{\text{[CII]}}$ is a viable way to derive molecular gas masses for $z \gtrsim 4$ non-AGN galaxies given its brightness and scaling relation between $L_{\text{[CII]}}$ and M_{H_2} calibrated on lower redshift samples. [CII] is expected to trace multiple gas phases (e.g., Maio et al. 2022; Maio & Viel 2023; Casavecchia et al. 2024), but the corresponding

emission is mostly due to the star formation activity in the host. As shown in the left panel of Fig. 2, $L_{\text{[CII]}}$ is tightly correlated (Pearson correlation coefficient ~ 0.71) with the SFR in quasar host galaxies at $z > 6$. The data points shown in Fig. 2 include all quasar at $z > 7$ and a collection of objects at $z \gtrsim 6$ from literature with both CO and [CII] measurements (see Table C.1 for the full list of objects and references). For this reason, several relations have been proposed to use the $L_{\text{[CII]}}$ to trace the molecular gas content based on the Kennicutt-Schmidt relation (Kennicutt 1998). As an example, the relation by Zanella et al. (2018) calibrated on main-sequence and starburst galaxies at redshift up to $z \sim 6$, with the bulk of the sample at $z \sim 2$. Alternatively, the relation by Madden et al. (2020) allows us to measure the total M_{H_2} , including the potential contribution due to CO-dark clouds, and is calibrated on local dwarf galaxies. As shown in the right panel of Fig. 2, both relations overestimate significantly the M_{H_2} measurement and upper limit derived from L_{CO} in quasars at $z > 5$. Indeed, several works in the literature studying the ISM properties of $z > 6$ quasars (e.g., Neeleman et al. 2021; Decarli et al. 2022; Kaasinen et al. 2024; Tripodi et al. 2024a) observed a large discrepancy between M_{H_2} derived with the prescription by Zanella et al. (2018) and Madden et al. (2020) and CO-derived ones, with [CII]-based M_{H_2} that overestimates CO-based M_{H_2} from a factor of a few to one order of magnitude (e.g., Kaasinen et al. 2024). The discrepancies in the determination of M_{H_2} from $L_{\text{[CII]}}$ are likely due to the different physical properties of the ISM between the sample collected by Zanella et al. (2018); Madden et al. (2020) and the host galaxies of high- z quasars. Indeed, when considering galaxies at high redshift ($z \gtrsim 4$) with an intense star formation activity (Rizzo et al. 2020, 2021), the measured M_{H_2} -to- $L_{\text{[CII]}}$ ratio is considerably lower ($\sim 4 - 8 M_{\odot}/L_{\odot}$) than the value $\sim 30 M_{\odot}/L_{\odot}$ measured by Zanella et al. (2018). This is also supported by the results of post-processed far-IR emission lines from the SIMBA cosmological hydrodynamical simulations (Vizgan et al. 2022), suggesting that the M_{H_2} -to- $L_{\text{[CII]}}$ ratio should be lowered up to a factor of ~ 2 for synthetic star-forming galaxies at $z \simeq 6$. Given that, we combine $L_{\text{[CII]}}$ and M_{H_2} measurements and upper limits for the $z > 7$ quasars presented in Table 2, with measurements for 21 $z \gtrsim 6$ quasars from the literature (see Table C.1) to provide a new calibration for the M_{H_2} - $L_{\text{[CII]}}$ relation. We fit data points of the resulting quasar sample of 25 objects with a linear regression based on a Bayesian approach, using the Python package *linmix* (Kelly 2007). This package allows us to consider errors on both variables, $L_{\text{[CII]}}$ and M_{H_2} , and upper limits on M_{H_2} . The best-fit relation is

$$\log(M_{H_2}/M_{\odot}) = (0.75_{-0.31}^{+0.31}) \log(L_{\text{[CII]}}) + (2.87_{-0.07}^{+0.07}) \quad (1)$$

and is shown in Fig. 2. The same relation corresponds roughly to a M_{H_2} -to- $L_{\text{[CII]}}$ ratio of $\sim 3.9_{-2.3}^{+1.7}$ in the $L_{\text{[CII]}}$ regime $10^9 - 10^{10} L_{\odot}$, almost one order of magnitude lower than that predicted by Zanella et al. (2018). We note that even if we consider a Milky Way like CO- H_2 conversion factor ($\alpha_{\text{CO}} = 4.3 M_{\odot} \text{pc}^{-2} (\text{K km s}^{-1})^{-1}$) to derive M_{H_2} for high- z quasars, the corresponding M_{H_2} would result lower by a factor 1.5-2 than those derived assuming the calibration of Zanella et al. (2018). This relation provides M_{H_2} estimates for luminous quasars ($L_{\text{bol}} > 10^{46}$ erg/s) at $z > 5$ that are way more accurate than those provided by scaling relation calibrated from star-forming or dwarf galaxies at lower redshift.

While applying this relation to high-redshift quasars, it is crucial to consider the following factors: (i) large-scale ionized winds driven by the accreting SMBH could significantly boost the observed $L_{\text{[CII]}}$ (e.g., Bischetti et al. 2024); (ii) tidally stripped gas

Table 2: Quasar properties

Name	ID	$\log M_{BH}$ M_{\odot}	$\log L_{bol}$ L_{\odot}	β	$\log M_{dust}$ M_{\odot}	$\log(L_{FIR})$ L_{\odot}	SFR $M_{\odot} \text{ yr}^{-1}$	$\log M_{H_2}$ M_{\odot}	Ref.
J0313-1806	J0313	9.2	13.6	1.6	$7.8^{+0.1}_{-0.2}$	$12.20^{+0.05}_{-0.05}$	160^{+20}_{-20}		1
J1243+0100	J1243	8.2	12.6	$1.97^{+0.19}_{-0.21}$	$8.0^{+0.2}_{-0.1}$	$12.68^{+0.06}_{-0.07}$	475^{+170}_{-160}	< 9.96	1
J0038-1527	J0038	9.3	13.7	1.6	$8.1^{+0.1}_{-0.1}$	$12.43^{+0.07}_{-0.07}$	270^{+75}_{-70}	< 10.16	1
J2356+0017	J2356			1.6	$8.0^{+0.1}_{-0.1}$	$12.56^{+0.07}_{-0.11}$	370^{+120}_{-110}	< 10.05	1
J0252-0503	J0252	9.3	13.5	$0.93^{+0.20}_{-0.21}$	$8.6^{+0.2}_{-0.1}$	$12.68^{+0.03}_{-0.03}$	476^{+36}_{-37}	< 10.14	1
J1120+0641	J1120	9.4	13.8		7.93 ± 0.03	$12.2^{+0.05}_{-0.03}$	220^{+15}_{-15}	< 9.5	2
J1007+2115	J1007	9.2	13.7		8.32 ± 12	12.2	165	10.26 ± 0.04	3,4
J1342+0928	J1342	8.9	13.6		7.54 ± 0.02	12	150	< 9.5	5

Notes. Quasars at $z > 7$ known to date (Fan et al. 2023). From left to right, columns include source name, ID adopted throughout the paper, logarithm of the BH mass, logarithm of bolometric luminosity, dust emissivity index, logarithm of the dust mass, and 40-1000 μ infrared luminosity, SFR and logarithm of the molecular gas mass. We refer to Table 1 in Fan et al. (2023) for the references for M_{BH} and L_{bol} for all $z > 7$ quasars. References for M_{H_2} , [CII], and IR measurements are (1) This work; (2) Venemans et al. (2017b); (3) Feruglio et al. (2023); (4) Yang et al. (2020); (5) (Novak et al. 2019)

due to merging companions close to the quasar (e.g., Tripodi et al. 2024b; Decarli et al. 2024) could enhance $L_{[CII]}$ measurements, especially in observations with limited angular resolution. Both (i) and (ii) cases could significantly overestimate the molecular gas masses in the quasar’s host galaxy.

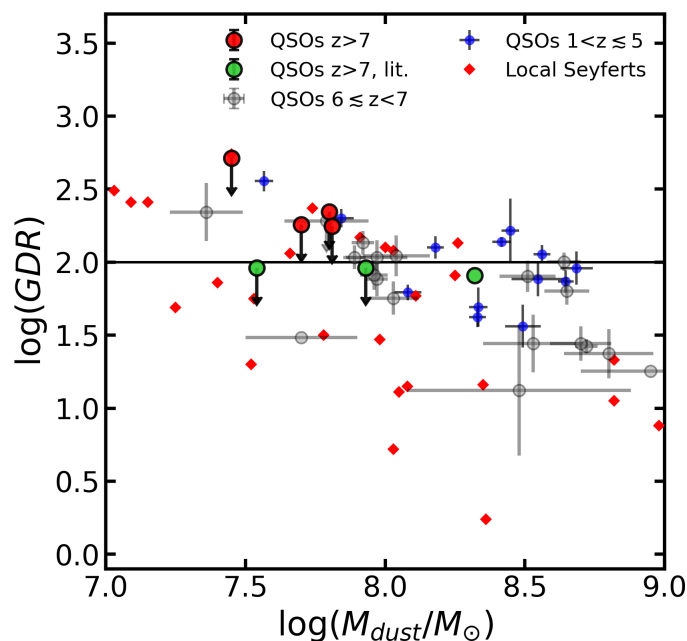


Fig. 3: Gas-to-dust ratio versus dust mass. The horizontal black line represents $GDR=100$. Red circles are the $z > 7$ quasars presented in this work with M_{H_2} upper limits. Green circles are for J1007 from Feruglio et al. (2023), J1120 from Venemans et al. (2017b), and J1342 from Novak et al. (2019). Grey circles are the $6 \leq z < 7$ quasars from Table C.1, while blue dots are for quasars at lower redshift are from (Bisetti et al. 2021; Decarli et al. 2022, and Salvestrini et al., in prep.). Local Seyfert galaxies are red diamonds.

4. Discussion

4.1. Dust enrichment at high-redshift

The origin of large dust reservoirs in the early Universe is widely debated (see Schneider & Maiolino 2024 for a comprehensive review on this topic), since there is no consensus on the dominant formation mechanisms. However, among the different channels for forming dust in the first few hundred million years of the Universe, Asymptotic Giant Branch (AGB) stars and Supernova (SN) ejecta are expected to contribute significantly even at $z > 7$ (e.g., Sommovigo et al. 2022). Even considering the maximally efficient yield from SN ejecta, this process can produce dust masses up to a few $10^7 M_{\odot}$ at the redshift of our targets (Mancini et al. 2015; Valiante et al. 2011). Nonetheless, we must also consider that a significant fraction of the dust created by SN ejecta (from 20% up to the total amount, depending on model assumptions; e.g., Micelotta et al. 2018; Kirchsclager et al. 2019) could be destroyed by the reverse shocks that may follow the initial explosion (Schneider & Maiolino 2024). Regarding AGB stars, their contribution to dust production depends mostly on the gas metallicity and the IMF (e.g., Ventura et al. 2018; Dell’Agli et al. 2019), nevertheless it can reach up to 40% of the total dust at $z \geq 6$ (e.g., Schneider & Maiolino 2024).

Moreover, two more processes are expected to significantly contribute to dust production in a pre-enriched ISM: aggregation and evolution of grains within the ISM, and quasar-driven winds. The aggregation of dust particles within the ISM usually requires time scales of the order of one Gyr and is observed to contribute up to 20-50% of the total dust production in the local Universe (Saintonge et al. 2018; Galliano et al. 2021). However, the extremely dense and turbulent ISM in the host galaxy of quasars (Gallerani et al. 2010; Valiante et al. 2011, 2014; Mancini et al. 2015; Decarli et al. 2023) could favor the formation of massive dust particles in a fraction of that time, making it the dominant channel in massive systems (e.g., Mancini et al. 2015). Indeed, local studies suggest that the aggregation of dust grains in the ISM primarily depends on gas density and temperature (e.g., Draine 2003, 2009; Galliano et al. 2021). Given the luminosity of the quasar at the EoR included in this study, we cannot exclude that a non-negligible amount of dust grains that are produced and continue to grow within the outflowing clouds that are ejected due to the SMBH feedback (Elvis et al. 2002). Even if the role of this production channel

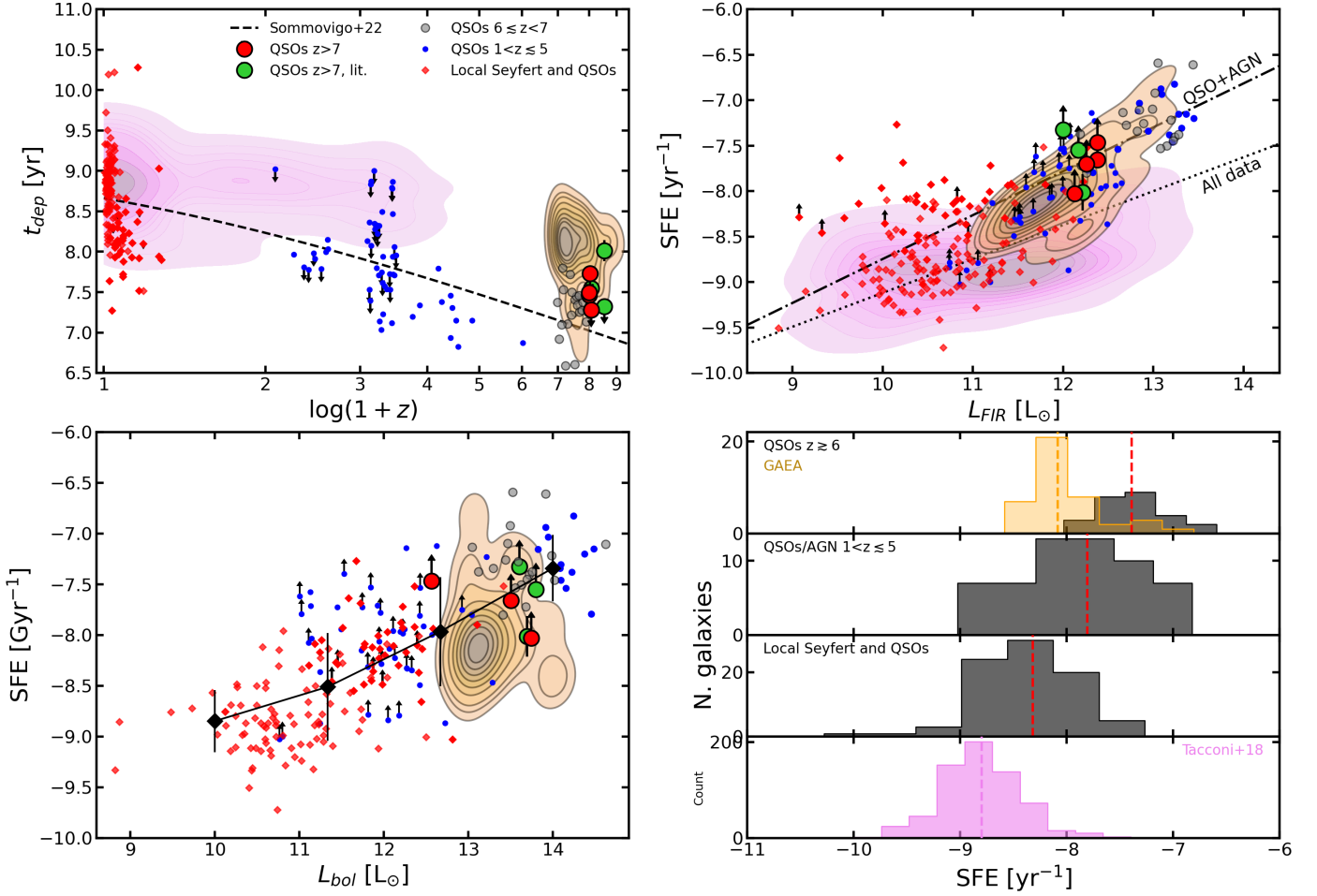


Fig. 4: Molecular gas consumption time scales and star formation efficiency. *Upper left panel:* The depletion time as a function of the logarithm of $(1+z)$. Sources are color-coded as follows: the $z > 7$ quasars are red (this work) and green (Venemans et al. 2017b; Novak et al. 2019; Feruglio et al. 2023) circles. Literature samples include: local (Saintonge et al. 2017, cyan shadowed region) and $z < 4$ (Tacconi et al. 2018, pink shadowed region) SFGs; local Seyfert galaxies and quasars (Bischetti et al. 2019b; Shangquan et al. 2020; Salvestrini et al. 2022; Salomé et al. 2023, red diamonds); quasars at Cosmic Noon (Bischetti et al. 2021; Bertola et al. 2024, blue dots); quasars at $6 \leq z < 7$ are gray circles (see Table C.1). The parameter space occupied by the simulated quasars from GAEA is shown as an orange-shaded region, with 10% isodensity lines. The dashed line represents the evolution of the depletion time with redshift (Sommovigo et al. 2022). *Upper right and lower left panels:* SFE is displayed as a function of L_{IR} (upper right) and L_{bol} (lower left), respectively. The best-fit lines are shown for illustration purposes only and were obtained from a linear fit of the data shown in the legend. Data points are color-coded as in the upper left panel. *Lower right panel:* The histograms of the SFE distribution of each sample are presented in the lower right panels, where the dashed line represents each distribution’s median value. The black diamonds represent the median SFE value in each of the equally spaced L_{bol} bins. The vertical lines represent the distance between the 84th and 16th percentile of the SFE distribution in each bin.

is still debated (e.g., Pipino et al. 2011), recent results from hydrodynamical simulations (Sarangi et al. 2019) suggest that this mechanism can be quite efficient (up to few $M_{\odot} \text{ yr}^{-1}$ for a $M_{\text{BH}} = 10^8 M_{\odot}$) in luminous quasars such as our targets. This means this channel can contribute to at least a few percent of the total dust budget, considering an AGN cycle of a million years. Although this makes dust production in quasar winds less significant compared to the other mechanisms just described, it could still play a crucial role in dust enrichment in nuclear regions.

To conclude, building dust masses that exceed $10^8 M_{\odot}$ in the host galaxies of luminous quasars at redshift $z > 7$ requires a combination of the physical processes described above.

As discussed above, the amount of dust traces the metal enrichment of the ISM. For this reason, the gas-to-dust ratio ($\text{GDR} = M_{\text{H}_2}/M_{\text{d}}$) is a crucial parameter to understand the rapid evolution and growth of galaxies at EoR. Here, we adopt the M_{H_2} measurement and upper limits listed in Table 2 to derive the GDR for 7 out of 8 quasars at $z > 7$, among which J1007 is the only object with a GDR estimate. We similarly derive GDRs for the quasars listed in Table C.1 and quasars with similar luminosity at Cosmic Noon from Bischetti et al. (2021). Since the high- z quasar population with dust mass estimates are biased towards luminous objects at far-IR wavelength, we also consider a sample of local Seyfert galaxies ($L_{\text{FIR}} \sim 10^{10-12} L_{\odot}$) to check for any potential selection bias. In Fig. 3, the resulting GDRs are shown as a function of M_{d} . Globally, the population of quasars at the EoR shows GDRs that are consistent

($GDR_{\text{mean}} = 75 \pm 40$) with the local value $GDR=100$ (Draine & Li 2007), similar to that measured in local star-forming galaxies (e.g., Casasola et al. 2020). This local value is commonly adopted also at high-redshift to derive the molecular gas mass given the dust mass (e.g., Neeleman et al. 2021). Among the quasars at $z > 7$, J1120 and J1342 show upper limits on GDR that are just below the local value ($\lesssim 90$). We remind that assuming a higher (lower) T_d value would result in a higher (lower) GDR up to a factor ~ 2 with $T_d = 65$ K (45 K). Looking at Fig. 3, GDR decreases at increasing M_d , with a similar trend in quasars and Seyfert galaxies. Indeed, by fitting the GDR versus M_d with LINMIX, we find a negative slope ($= 1 \pm 0.07$) when considering only quasars at the EoR. Consistent results can be obtained by either including lower redshift quasars and local Seyfert galaxies (in the former case, there is a shift in the normalization). This trend is likely driven by the level of metal enrichment of the ISM, since gas-phase metallicity is considered to be the main physical properties driving the GDR (Rémy-Ruyer et al. 2014). This confirms that dust-rich systems are already enriched in metals, which contribute to the formation of dust particles. However, we remind that our M_{H_2} estimates are derived with a constant α_{CO} factor, while an assumption of α_{CO} dependent on metallicity (e.g., Amorín et al. 2016) would have balanced out the GDR anti-correlation with M_d . We conclude that quasars at the EoR exhibit GDR values (both detection and upper limits) consistent with those measured in quasars at lower redshift and in local objects. This confirms that assuming a local GDR value (Draine & Li 2007) is a reasonable choice for quasar host galaxies up to $z \sim 7.5$.

4.2. Gas depletion and star formation efficiency

In the top left panel of Fig. 4, we show the depletion time ($t_{\text{dep}} = M_{H_2}/SFR$) as a function of redshift. As a comparison, we include a collection of quasars spanning a wide range of redshift, namely: quasars at $6 \lesssim z < 7$ (see Table C.1), luminous objects at Cosmic Noon from (Bischetti et al. 2018, 2021; Decarli et al. 2022; Bertola et al. 2024, Salvestrini et al., in prep.), and in the nearby Universe (Bischetti et al. 2019b; Shangguan et al. 2020, PDS456 and the PG survey, respectively). We also extend the comparison to AGN at intermediate luminosities ($L_{\text{bol}} \sim 10^{44-45}$ erg/s), with samples of local AGN/Seyfert galaxies from Koss et al. (2021); Salvestrini et al. (2022) and highly accreting AGN from Salomé et al. (2023). Eventually, we add star-forming and luminous infrared galaxies with CO detections from (Tacconi et al. 2018), which cover a wide range of redshift, from the nearby Universe up to redshift $z \sim 4$. As clearly visible, the quasars at the EoR show relatively low ($t_{\text{dep}} \lesssim 0.1$ Gyr), with few objects reaching depletion times of a few tens on Myr. If we limit the analysis to the EoR, there is no evidence for the evolution of t_{dep} in quasar host galaxies.

To further investigate this scenario, we contrast our findings against theoretical predictions from the GALaxy Evolution and Assembly (GAEA) model. In particular, the latest rendition of the model (De Lucia et al. 2024) combines the explicit partitioning of the cold gas into its molecular and neutral phases (the molecular gas ratio depends on the mid-plane pressure Blitz & Rosolowsky 2006, more details in Xie et al. 2017), with improved modeling of AGN activity (both in terms of cold gas accretion onto SMBHs and AGN-driven feedback Fontanot et al. 2020). The GAEA semi-analytic model (SAM) has been recently (Fontanot et al., in prep.) coupled to the P-MILLENNIUM simulation (Baugh et al. 2019), that spans a volume of 800^3 Mpc³, with a mass resolution of $m_p = 1.06 \times 10^8 M_\odot$, and assuming cosmo-

logical parameters consistent with the first year results from the Planck satellite (Planck Collaboration et al. 2014), to predict the evolution of galaxy properties from $z \sim 20$ to the local Universe (Cantarella et al., in prep.). We extracted all predicted AGN from the simulated box with a $L_{\text{bol}} > 3 \times 10^{46}$ erg s⁻¹ at $z > 6$, resulting in a sample of 42 individual sources. For each of these sources, we study their mean molecular gas content and SFR, by considering the evolution of these quantities over a timescale compatible with the Eddington time ($\sim 4 \times 10^7$ yrs), before the peak of the predicted AGN activity. The synthetic objects show a distribution of t_{dep} that covers a larger range of values, with the bulk of the population of 42 GAEA quasars that have depletion times of a few hundred million years. This can be due to the prescription used in the GAEA SAM that instantaneously triggers the quasar phase when a sufficient amount of gas is concentrated in a certain radius in the host galaxy. This favors the emergence of bright quasars, as well as the case of less massive objects, with respect to our current picture of bright quasars. Indeed, GAEA quasars show M_{BH} that is roughly two orders of magnitude smaller ($\log(M_{BH}/M_\odot \sim 7.40 \pm 0.23$) than that observed in the quasar at redshift $z > 6$ ($\log(M_{BH}/M_\odot \sim 9.33 \pm 0.24$). This is likely due to the flat prescription adopted for BH seeding, which does not consider the hypothesis that massive ($M_{BH} > 10^6 M_\odot$) can form via the direct collapse of giant gas clouds in the early Universe (for an alternative approach, see Trinca et al. 2022). Furthermore, the different distribution between synthetic and observed quasars can be partially due to an observational bias because we only detect the brightest sources at the EoR. Indeed, considering the quasars at Cosmic Noon which span a larger regime L_{bol} and L_{FIR} (see upper right and lower left panels of Fig. 4), quasars from the SUPER and KASHz samples by Bertola et al. (2024) show depletion times that are consistent with the bulk of GAEA objects. Eventually, AGN and star-forming galaxies at lower redshift show a wider range of t_{dep} value, but the bulk of the distributions peak close to $t_{\text{dep}} \sim 1$ Gyr.

An interpretation of this result requires that the feedback from the SMBH in high-redshift and luminous quasars can remove or heat the cold gas reservoir from their host (Brusa et al. 2018; Fiore et al. 2017; Fluetsch et al. 2019). However, several studies of SMBH-driven winds in quasars at different redshifts have shown that they are not powerful enough to impact the star formation (Bischetti et al. 2019a; Tripodi et al. 2023; Novak et al. 2019), at least in the cold phase of the gas. Indeed, simulations (Costa et al. 2020, 2022; Valentini et al. 2021) suggest that the quenching effect of the accreting SMBH is not instantaneously effective, hence accretion onto the SMBH and massive star formation coexist.

A different interpretation proposes that the relatively low depletion times are likely due to the highly efficient star formation of the quasar host that is favored by the concentration of cold gas in a relatively compact size. To discuss this scenario, we then derive the gas star formation efficiency, defined as $SFE_{\text{gas}} = 1/t_{\text{dep}} = SFR/M(H_2)$ (SFE, hereafter), that is represented as a function of L_{IR} in the upper right panel of Fig. 4. The trend between SFE and L_{FIR} shown in the upper right panel of Fig. 4 suggests that the galaxies that are brighter at far-IR wavelengths (hence have higher SFR), are relatively more efficient at forming stars when compared to galaxies at lower L_{FIR} . This is true, irrespective of the presence of a quasar/AGN at their center. Nonetheless, quasar hosts exceed up to one order of magnitude the SFE measured in star-forming and luminous galaxies (Tacconi et al. 2018; dash-dotted and dotted lines in the upper panel of Fig. 4) at high luminosities ($L_{\text{FIR}} > 10^{12} L_\odot$). In particular,

quasars at the EoR show the highest efficiencies among the objects considered in our analysis, except for the hyper-luminous quasars at Cosmic Noon from the WISSH sample (Bischetti et al. 2021, Salvestrini et al. in prep.). Regarding $z > 7$ massive quasar hosts, we find lower limits $SFE > 10^{-8} \text{ yr}^{-1}$, slightly larger than the SFE measured in J1007 $SFE = 9.7 \pm 2.5 \times 10^{-9} \text{ yr}^{-1}$.

As discussed in section 3.2, a highly star-forming host galaxy is a common characteristic among bright ($L_{bol} > 10^{12.5} L_{\odot}$) quasars at high-redshift (e.g., Venemans et al. 2017a; Decarli et al. 2022; Izumi et al. 2021; Tripodi et al. 2024a). However, this effect could result from a combination of observational bias and the evolution of the Main Sequence (MS; Renzini & Peng 2015) at high redshift. Regarding the first point, we still lack a complete sampling, especially at (sub)-mm wavelengths, of galaxy populations at intermediate luminosities ($L_{FIR} < 10^{12} L_{\odot}$). Concerning the second point, the SFR is expected to increase for MS galaxies with redshift as a result of the higher cosmological accretion rate at early times ($0 < z < 6$; Tacconi et al. 2020; Walter et al. 2020; Popesso et al. 2023). This is confirmed by observational studies (e.g., Tacconi et al. 2020; Sommovigo et al. 2022) which found that the depletion time decreases with redshift, with values of ~ 0.01 Gyr at $z \sim 7$, consistent with those observed in quasars at the EoR (see the upper left panel of Fig. 4). These two points should be taken into account when interpreting the lower right panel of Fig. 4. In each histogram, AGN/quasar sources are divided by redshift, while the luminous and star-forming galaxies from Tacconi et al. (2018) are shown for comparison in the lower panel. Quasars at the EoR represent only the population of the brightest sources at this epoch, and we are likely missing the rich population of intermediate luminosity AGN recently discovered with JWST (e.g., Harikane et al. (2023); Maiolino et al. (2024b,a)). In this regard, the results from the GAEA simulations predict a broader distribution of SFE, with a peak at lower SFE with respect to observations of quasars at similar redshift. Thanks to JWST, it is now possible to detect the stellar light from the quasar host (Ding et al. 2023), and to model the corresponding emission to derive stellar masses (e.g., Ding et al. 2023; Yue et al. 2024). We take the estimate and upper limit of the stellar mass from Yue et al. (2024) for four quasars at the EoR, among which J1120 and three other quasars are listed in Table C.1. We then calculate the specific SFR ($sSFR = SFR/M_{\star}$) and molecular gas fraction ($f_{gas} = M_{H2}/M_{\star}$). The lower limit and estimate of the sSFR ($> 10^{-8} \text{ yr}^{-1}$) are way above the expected value for main sequence galaxies at the EoR. Their molecular gas fraction ($f_{gas} \sim 0.05 - 0.5$) is lower than what observed in local quasars and AGN (Shangguan et al. 2020; Salvestrini et al. 2022), but consistent with that derived from dynamical measurements in luminous quasars at Cosmic Noon (Bischetti et al. 2021). This confirms that these objects are experiencing an intense starburst phase which is coeval with the bright phase of the quasars, justifying the shift between the median value of the SFE distribution between AGN and non-AGN host galaxies in the histograms of Fig. 4.

In the lower-left panel of Fig. 4, we show the SFE as a function of the bolometric luminosity of the accreting SMBH. The black solid line connects the median value of the SFE of quasars and AGN divided into four bins of L_{bol} . The increasing trend between the SFE and L_{bol}^5 shown in the lower left panel of Fig. 4 suggests that the processes that convey a significant amount of gas toward the nuclear region (e.g., disc instabilities) are more

efficient than the effect of the feedback (e.g., outflows) produced by the accreting SMBH, which is expected to be proportional to the quasar luminosity (Fiore et al. 2017; Fluetsch et al. 2019). We then conclude that among the known population of bright quasars at the EoR there is no clear evidence for an efficient quenching of the host-galaxy star formation due to quasar feedback. On the contrary, at such early epochs, a bright quasar phase is likely coeval with an intense build-up phase in the host galaxy. The coexistence between SMBH growth and intense star formation in the host is visible at all redshifts, when considering luminous quasars, suggesting that quasar activity benefits from the gas concentration in the nuclear region of the galaxy. An alternative scenario can be that the quasar activity triggers the star formation in the host, by compressing the gas in the surrounding medium (Cresci & Maiolino 2018).

5. Conclusions

In this work, we present new NOEMA observations targeting CO emission lines for five $z > 7$ quasars, completing the survey of molecular gas properties for all eight known quasars at this epoch. These observations represent the highest redshift investigation of cold dust and gas to date in a sample of quasar host galaxies at the EoR. By modeling the far-IR emission with a modified black body using EoS-DUSTFIT, we derive dust properties and SFR estimates for our sample. Although no statistically significant CO emission lines were detected in the five targets, we derive upper limits on the molecular gas mass. In the analysis presented above, we compare the molecular gas and dust properties of all known $z > 7$ quasars with a compilation of quasar hosts and star-forming galaxies at different redshifts. Our results are:

- Among the eight known quasars at $z > 7$, only one object (J1007; Feruglio et al. 2023) has a statistically significant estimate of the molecular gas mass. Here, we find no massive gas reservoirs ($M_{H2} < \text{few} 10^{10} M_{\odot}$) at $z > 7$.
- Combining the new observations presented in this work with measurements from the literature, we provide a new calibration to derive M_{H2} from $L_{[CII]}$ for $z \geq 6$ quasars.
- Quasar host galaxies at $z > 7$ have already built large dust reservoirs ($M_{dust} \sim 10^8 M_{\odot}$) in a relatively short time (a few hundred Myr) after the Big Bang. This suggests that the physical processes responsible for dust enrichment are very efficient, which may include contributions from evolved stellar populations, SN, and reprocessing within the ISM. The GDR estimate and upper limits for $z > 7$ quasars presented here align with the mean gas-to-dust ratio (GDR) for luminous quasars and AGN at later epochs, which is consistent with the local value (GDR=100, Draine & Li 2007).
- Quasars at the EoR are hosted in galaxies undergoing intense starburst phases, with SFEs up to an order of magnitude higher than those expected for non-AGN host galaxies. This suggests that the emergence of a luminous quasar phase is coeval with the rapid build-up of the host galaxy.
- Semi-analytical models of quasar host galaxies from GAEA at the EoR also support the idea that the quasar phase is triggered during periods of efficient star formation.

Acknowledgements. The project leading to this publication has received support from ORP, that is funded by the European Union’s Horizon 2020 research and innovation programme under grant agreement No 101004719 [ORP]. This work is based on observations carried out under project number S23CX with the IRAM NOEMA Interferometer. IRAM is supported by INSU/CNRS (France), MPG (Germany) and IGN (Spain). LZ, EP, AT, and FS acknowledge financial support from the Bando Ricerca Fondamentale INAF 2022 Large Grant “Toward

⁵ The Pearson correlation coefficient for the SFE- L_{bol} relation is 0.53 and 0.46 considering all quasars at $z > 1$ or the all AGN and quasars shown in the plot, respectively.

an holistic view of the Titans: multi-band observations of $z > 6$ QSOs powered by greedy supermassive black holes". CF, and FS acknowledge financial support from PRIN MUR 2022 2022TKPB2P - BIG-z and Ricerca Fondamentale INAF 2023 Data Analysis grant "ARCHIE ARchive Cosmic HI & ISM Evolution". M.B. acknowledges support from INAF under project 1.05.12.04.01 - 431 MINI-GRANTS di RSN1 "Mini-feedback" and support from UniTs under project DF-microgrants23 "Hyper-Gal". This paper makes use of the following ALMA data: ADS/JAO.ALMA#2018.1.01188.S, #2019.A.00017.S, #2019.1.00074.S, #2019.1.01025.S, #2021.1.00934.S, #2021.1.01262.S. ALMA is a partnership of ESO (representing its member states), NFS (USA) and NINS (Japan), together with NRC (Canada), MOST and ASIAA (Taiwan) and KASI (Republic of Korea), in cooperation with the Republic of Chile. The Joint ALMA Observatory is operated by ESO, AUI/NRAO and NAOJ. *Software*: *Astropy* (*Astropy Collaboration et al.* 2013, 2018, 2022); *CASA* (*CASA Team et al.* 2022); *EMCEE* (*Foreman-Mackey et al.* 2013, 2019); *GILDAS* <https://www.iram.fr/IRAMFR/GILDAS/>; *LINMIX* (*Kelly* 2007); *MATPLOTLIB* (*Hunter* 2007); *NUMPY* (*Harris et al.* 2020); *SEABORN* (*Waskom* 2021); *SCIPY* (*Virtanen et al.* 2020).

References

- Algera, H. S. B., Inami, H., Sommovigo, L., et al. 2024, *MNRAS*, 527, 6867
- Amorín, R., Muñoz-Tuñón, C., Aguerri, J. A. L., & Planesas, P. 2016, *A&A*, 588, A23
- Astropy Collaboration*, Price-Whelan, A. M., Lim, P. L., et al. 2022, *ApJ*, 935, 167
- Astropy Collaboration*, Price-Whelan, A. M., Sipőcz, B. M., et al. 2018, *AJ*, 156, 123
- Astropy Collaboration*, Robitaille, T. P., Tollerud, E. J., et al. 2013, *A&A*, 558, A33
- Bañados, E., Venemans, B. P., Decarli, R., et al. 2016, *ApJS*, 227, 11
- Baugh, C. M., Gonzalez-Perez, V., Lagos, C. D. P., et al. 2019, *MNRAS*, 483, 4922
- Beelen, A., Cox, P., Benford, D. J., et al. 2006, *ApJ*, 642, 694
- Bertola, E., Circosta, C., Ginolfi, M., et al. 2024, *A&A*, 691, A178
- Bischetti, M., Choi, H., Fiore, F., et al. 2024, *ApJ*, 970, 9
- Bischetti, M., Feruglio, C., Piconcelli, E., et al. 2021, *A&A*, 645, A33
- Bischetti, M., Maiolino, R., Carniani, S., et al. 2019a, *A&A*, 630, A59
- Bischetti, M., Piconcelli, E., Feruglio, C., et al. 2018, *A&A*, 617, A82
- Bischetti, M., Piconcelli, E., Feruglio, C., et al. 2019b, *A&A*, 628, A118
- Blitz, L. & Rosolowsky, E. 2006, *ApJ*, 650, 933
- Bolatto, A. D., Wolfire, M., & Leroy, A. K. 2013, *ARA&A*, 51, 207
- Brusa, M., Cresci, G., Daddi, E., et al. 2018, *A&A*, 612, A29
- Carilli, C. L. & Walter, F. 2013, *ARA&A*, 51, 105
- Carniani, S., Gallerani, S., Vallini, L., et al. 2019, *MNRAS*, 489, 3939
- CASA Team, Bean, B., Bhatnagar, S., et al. 2022, *PASP*, 134, 114501
- Casasola, V., Bianchi, S., De Vis, P., et al. 2020, *A&A*, 633, A100
- Casavecchia, B., Maio, U., Péroux, C., & Ciardi, B. 2024, arXiv e-prints, arXiv:2410.14284
- Chabrier, G. 2003, *PASP*, 115, 763
- Costa, T., Arrigoni Battaia, F., Farina, E. P., et al. 2022, *MNRAS*, 517, 1767
- Costa, T., Pakmor, R., & Springel, V. 2020, *MNRAS*, 497, 5229
- Cresci, G. & Maiolino, R. 2018, *Nature Astronomy*, 2, 179
- De Looze, I., Cormier, D., Lebouteiller, V., et al. 2014, *A&A*, 568, A62
- De Lucia, G., Fontanot, F., Xie, L., & Hirschmann, M. 2024, *A&A*, 687, A68
- Decarli, R., Loiacono, F., Farina, E. P., et al. 2024, *A&A*, 689, A219
- Decarli, R., Pensabene, A., Diaz-Santos, T., et al. 2023, *A&A*, 673, A157
- Decarli, R., Pensabene, A., Venemans, B., et al. 2022, *A&A*, 662, A60
- Decarli, R., Walter, F., Venemans, B. P., et al. 2017, *Nature*, 545, 457
- Decarli, R., Walter, F., Venemans, B. P., et al. 2018, *ApJ*, 854, 97
- Dell'Agli, F., Valiante, R., Kamath, D., Ventura, P., & García-Hernández, D. A. 2019, *MNRAS*, 486, 4738
- Di Mascia, F., Gallerani, S., Behrens, C., et al. 2021, *MNRAS*, 503, 2349
- Dietrich, M. & Hamann, F. 2004, *ApJ*, 611, 761
- Ding, X., Onoue, M., Silverman, J. D., et al. 2023, *Nature*, 621, 51
- Draine, B. T. 2003, *ARA&A*, 41, 241
- Draine, B. T. 2009, in *Astronomical Society of the Pacific Conference Series*, Vol. 414, *Cosmic Dust - Near and Far*, ed. T. Henning, E. Grün, & J. Steinacker, 453
- Draine, B. T. & Li, A. 2007, *ApJ*, 657, 810
- Duras, F., Bongiorno, A., Piconcelli, E., et al. 2017, *A&A*, 604, A67
- Elvis, M., Marengo, M., & Karovska, M. 2002, *ApJ*, 567, L107
- Fan, X., Bañados, E., & Simcoe, R. A. 2023, *ARA&A*, 61, 373
- Feruglio, C., Fiore, F., Carniani, S., et al. 2018, *A&A*, 619, A39
- Feruglio, C., Maio, U., Tripodi, R., et al. 2023, *ApJ*, 954, L10
- Fiore, F., Feruglio, C., Shankar, F., et al. 2017, *A&A*, 601, A143
- Fluetsch, A., Maiolino, R., Carniani, S., et al. 2019, *MNRAS*, 483, 4586
- Fontanot, F., De Lucia, G., Hirschmann, M., et al. 2020, *MNRAS*, 496, 3943
- Foreman-Mackey, D., Farr, W., Sinha, M., et al. 2019, *The Journal of Open Source Software*, 4, 1864
- Foreman-Mackey, D., Hogg, D. W., Lang, D., & Goodman, J. 2013, *PASP*, 125, 306
- Gallerani, S., Maiolino, R., Juarez, Y., et al. 2010, *A&A*, 523, A85
- Galliano, F., Nersesian, A., Bianchi, S., et al. 2021, *A&A*, 649, A18
- Gunn, J. E. & Peterson, B. A. 1965, *ApJ*, 142, 1633
- Harikane, Y., Zhang, Y., Nakajima, K., et al. 2023, *ApJ*, 959, 39
- Harris, C. R., Millman, K. J., van der Walt, S. J., et al. 2020, *Nature*, 585, 357
- Herrera-Camus, R., Sturm, E., Graciá-Carpio, J., et al. 2018, *ApJ*, 861, 95
- Hunter, J. D. 2007, *Computing in Science & Engineering*, 9, 90
- Hygate, A. P. S., Hodge, J. A., da Cunha, E., et al. 2023, *MNRAS*, 524, 1775
- Izumi, T., Matsuoka, Y., Fujimoto, S., et al. 2021, *ApJ*, 914, 36
- Izumi, T., Matsuoka, Y., Onoue, M., et al. 2024, *ApJ*, 972, 116
- Kaasinen, M., Venemans, B., Harrington, K. C., et al. 2024, *A&A*, 684, A33
- Kashikawa, N., Ishizaki, Y., Willott, C. J., et al. 2015, *ApJ*, 798, 28
- Kelly, B. C. 2007, *ApJ*, 665, 1489
- Kennicutt, Robert C., J. 1998, *ARA&A*, 36, 189
- Kirschlagler, F., Schmidt, F. D., Barlow, M. J., et al. 2019, *MNRAS*, 489, 4465
- Koss, M. J., Strittmatter, B., Lamperti, I., et al. 2021, *ApJS*, 252, 29
- Kroupa, P. 2001, *MNRAS*, 322, 231
- Leńniewska, A. & Michałowski, M. J. 2019, *A&A*, 624, L13
- Madden, S. C., Cormier, D., Hony, S., et al. 2020, *A&A*, 643, A141
- Maio, U., Péroux, C., & Ciardi, B. 2022, *A&A*, 657, A47
- Maio, U. & Viel, M. 2023, *A&A*, 672, A71
- Maiolino, R., Cox, P., Caselli, P., et al. 2005, *A&A*, 440, L51
- Maiolino, R., Risaliti, G., Signorini, M., et al. 2024a, arXiv e-prints, arXiv:2405.00504
- Maiolino, R., Scholtz, J., Curtis-Lake, E., et al. 2024b, *A&A*, 691, A145
- Mancini, M., Schneider, R., Graziani, L., et al. 2015, *MNRAS*, 451, L70
- Mazzucchelli, C., Bañados, E., Venemans, B. P., et al. 2017, *ApJ*, 849, 91
- McMullin, J. P., Waters, B., Schiebel, D., Young, W., & Golap, K. 2007, in *Astronomical Society of the Pacific Conference Series*, Vol. 376, *Astronomical Data Analysis Software and Systems XVI*, ed. R. A. Shaw, F. Hill, & D. J. Bell, 127
- Micelotta, E. R., Matsuura, M., & Sarangi, A. 2018, *Space Sci. Rev.*, 214, 53
- Neeleman, M., Bañados, E., Walter, F., et al. 2019, *The Astrophysical Journal*, 882, 10
- Neeleman, M., Novak, M., Venemans, B. P., et al. 2021, *ApJ*, 911, 141
- Novak, M., Bañados, E., Decarli, R., et al. 2019, *ApJ*, 881, 63
- Pensabene, A., van der Werf, P., Decarli, R., et al. 2022, *A&A*, 667, A9
- Pineda, J. L., Langer, W. D., Velusamy, T., & Goldsmith, P. F. 2013, *A&A*, 554, A103
- Pipino, A., Fan, X. L., Matteucci, F., et al. 2011, *A&A*, 525, A61
- Planck Collaboration, Ade, P. A. R., Aghanim, N., et al. 2014, *A&A*, 571, A16
- Poppo, P., Concas, A., Cresci, G., et al. 2023, *MNRAS*, 519, 1526
- Popping, G., Somerville, R. S., & Galametz, M. 2017, *MNRAS*, 471, 3152
- Pozzi, F., Calura, F., Fudamoto, Y., et al. 2021, *A&A*, 653, A84
- Rémy-Ruyer, A., Madden, S. C., Galliano, F., et al. 2014, *A&A*, 563, A31
- Renzini, A. & Peng, Y.-j. 2015, *ApJ*, 801, L29
- Riechers, D. A., Walter, F., Bertoldi, F., et al. 2009, *ApJ*, 703, 1338
- Riechers, D. A., Walter, F., Carilli, C. L., & Bertoldi, F. 2007, *ApJ*, 671, L13
- Riechers, D. A., Walter, F., Carilli, C. L., et al. 2006, *ApJ*, 650, 604
- Rizzo, F., Vegetti, S., Fraternali, F., Stacey, H. R., & Powell, D. 2021, *MNRAS*, 507, 3952
- Rizzo, F., Vegetti, S., Powell, D., et al. 2020, *Nature*, 584, 201
- Romano, M., Morselli, L., Cassata, P., et al. 2022, *A&A*, 660, A14
- Ronconi, T., Lapi, A., Torsello, M., et al. 2024, *A&A*, 685, A161
- Saintonge, A., Catinella, B., Tacconi, L. J., et al. 2017, *ApJS*, 233, 22
- Saintonge, A., Wilson, C. D., Xiao, T., et al. 2018, *MNRAS*, 481, 3497
- Salomé, Q., Krongold, Y., Longinotti, A. L., et al. 2023, *MNRAS*, 524, 3130
- Salvestrini, F., Gruppioni, C., Hatziminaoglou, E., et al. 2022, *A&A*, 663, A28
- Sarangi, A., Dwek, E., & Kazanas, D. 2019, *ApJ*, 885, 126
- Schneider, R. & Maiolino, R. 2024, *A&A Rev.*, 32, 2
- Shangguan, J., Ho, L. C., Bauer, F. E., Wang, R., & Treister, E. 2020, *ApJ*, 899, 112
- Shao, Y., Wang, R., Weiss, A., et al. 2022, *A&A*, 668, A121
- Shen, Y., Richards, G. T., Strauss, M. A., et al. 2011, *ApJS*, 194, 45
- Shen, Y., Wu, J., Jiang, L., et al. 2019, *ApJ*, 873, 35
- Sommovigo, L., Ferrara, A., Pallottini, A., et al. 2022, *MNRAS*, 513, 3122
- Stefan, I. I., Carilli, C. L., Wagg, J., et al. 2015, *MNRAS*, 451, 1713
- Tacconi, L. J., Genzel, R., Saintonge, A., et al. 2018, *ApJ*, 853, 179
- Tacconi, L. J., Genzel, R., & Sternberg, A. 2020, *ARA&A*, 58, 157
- Trinca, A., Schneider, R., Valiante, R., et al. 2022, *MNRAS*, 511, 616
- Tripodi, R., Feruglio, C., Fiore, F., et al. 2024a, *A&A*, 689, A220
- Tripodi, R., Feruglio, C., Kemper, F., et al. 2023, *ApJ*, 946, L45
- Tripodi, R., Scholtz, J., Maiolino, R., et al. 2024b, *A&A*, 682, A54
- Tsukui, T., Wisnioski, E., Krumholz, M. R., & Battisti, A. 2023, *MNRAS*, 523, 4654
- Valentini, M., Gallerani, S., & Ferrara, A. 2021, *MNRAS*, 507, 1

- Valiante, R., Schneider, R., Salvadori, S., & Bianchi, S. 2011, MNRAS, 416, 1916
- Valiante, R., Schneider, R., Salvadori, S., & Gallerani, S. 2014, MNRAS, 444, 2442
- Venemans, B. P., Neeleman, M., Walter, F., et al. 2019, ApJ, 874, L30
- Venemans, B. P., Walter, F., Decarli, R., et al. 2017a, ApJ, 851, L8
- Venemans, B. P., Walter, F., Decarli, R., et al. 2017b, ApJ, 837, 146
- Venemans, B. P., Walter, F., Decarli, R., et al. 2017c, ApJ, 845, 154
- Venemans, B. P., Walter, F., Neeleman, M., et al. 2020, ApJ, 904, 130
- Ventura, P., Karakas, A., Dell’Agli, F., García-Hernández, D. A., & Guzman-Ramirez, L. 2018, MNRAS, 475, 2282
- Virtanen, P., Gommers, R., Oliphant, T. E., et al. 2020, Nature Methods, 17, 261
- Vizgan, D., Greve, T. R., Olsen, K. P., et al. 2022, ApJ, 929, 92
- Walter, F., Carilli, C., Neeleman, M., et al. 2020, ApJ, 902, 111
- Walter, F., Neeleman, M., Decarli, R., et al. 2022, ApJ, 927, 21
- Wang, F., Yang, J., Fan, X., et al. 2021, ApJ, 907, L1
- Wang, F., Yang, J., Fan, X., et al. 2024, ApJ, 968, 9
- Wang, R., Carilli, C. L., Beelen, A., et al. 2007, AJ, 134, 617
- Wang, R., Carilli, C. L., Neri, R., et al. 2010, ApJ, 714, 699
- Wang, R., Wagg, J., Carilli, C. L., et al. 2011, AJ, 142, 101
- Wang, R., Wagg, J., Carilli, C. L., et al. 2013, ApJ, 773, 44
- Waskom, M. L. 2021, Journal of Open Source Software, 6, 3021
- Witstok, J., Jones, G. C., Maiolino, R., Smit, R., & Schneider, R. 2023, MNRAS, 523, 3119
- Witstok, J., Smit, R., Maiolino, R., et al. 2022, MNRAS, 515, 1751
- Xie, L., De Lucia, G., Hirschmann, M., Fontanot, F., & Zoldan, A. 2017, MNRAS, 469, 968
- Yang, J., Wang, F., Fan, X., et al. 2021, ApJ, 923, 262
- Yang, J., Wang, F., Fan, X., et al. 2020, ApJ, 897, L14
- Yue, M., Eilers, A.-C., Simcoe, R. A., et al. 2024, ApJ, 966, 176
- Zanella, A., Daddi, E., Magdis, G., et al. 2018, MNRAS, 481, 1976

Appendix A: Far-infrared SED models

In Fig. A.1, we present the best-fit models of the far-IR SED of the five quasars at $z > 7$ in our sample. The corresponding corner plots of the free parameters obtained with the Bayesian analysis of the MBB with the EOS-DUSTFIT code are shown in Fig. A.2. Details of the analysis are reported in section 3.1.

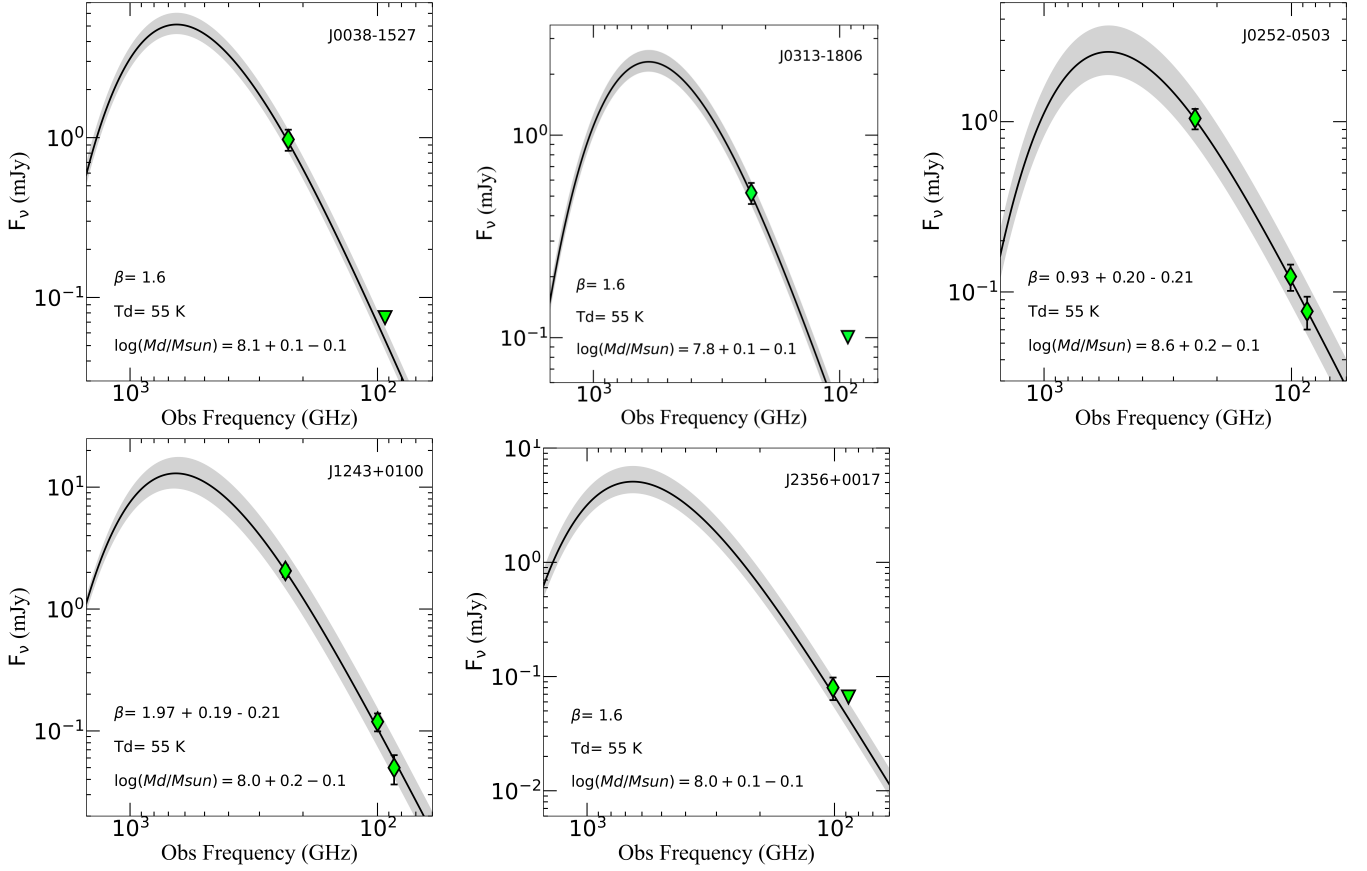


Fig. A.1: Far-infrared spectral energy distribution. Observed fluxes and upper limits are shown as green diamonds and triangles, respectively. The best-fit model is the black line, and the corresponding parameters (namely β , T_d , and M_d) are reported in each panel.

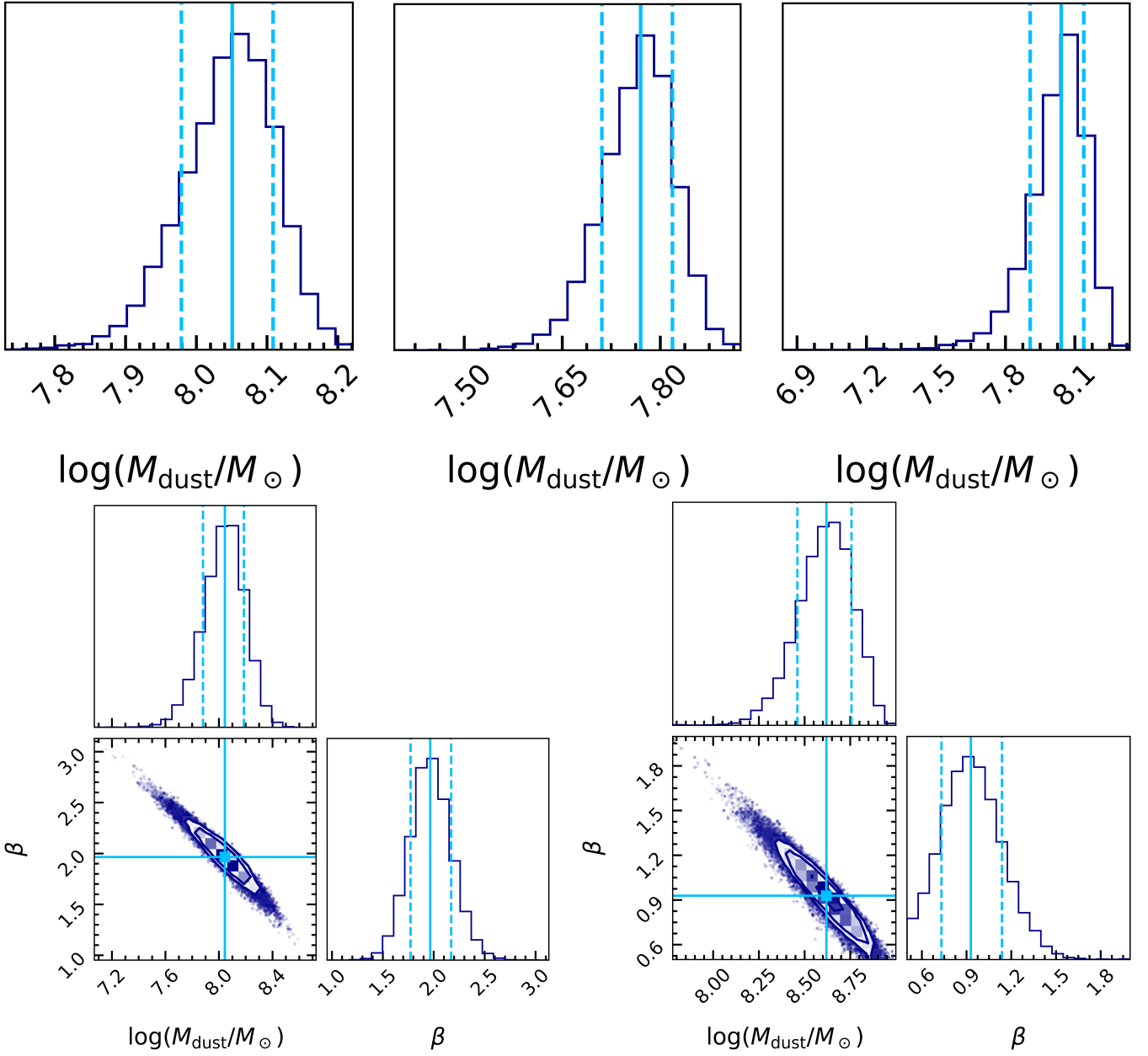


Fig. A.2: Corner plots showing the posterior probability distributions of M_d and β (only for J0252 and J1243, lower panels). Cyan solid lines indicate the best-fitting value for each parameter, while the dashed lines mark each parameter's 16th and 84th percentiles.

Appendix B: Continuum maps

In Fig. B.1 we present the continuum maps produced from the interferometric data collected and analyzed as described in section 2. Flux densities were extracted from the continuum maps as described in section 2.

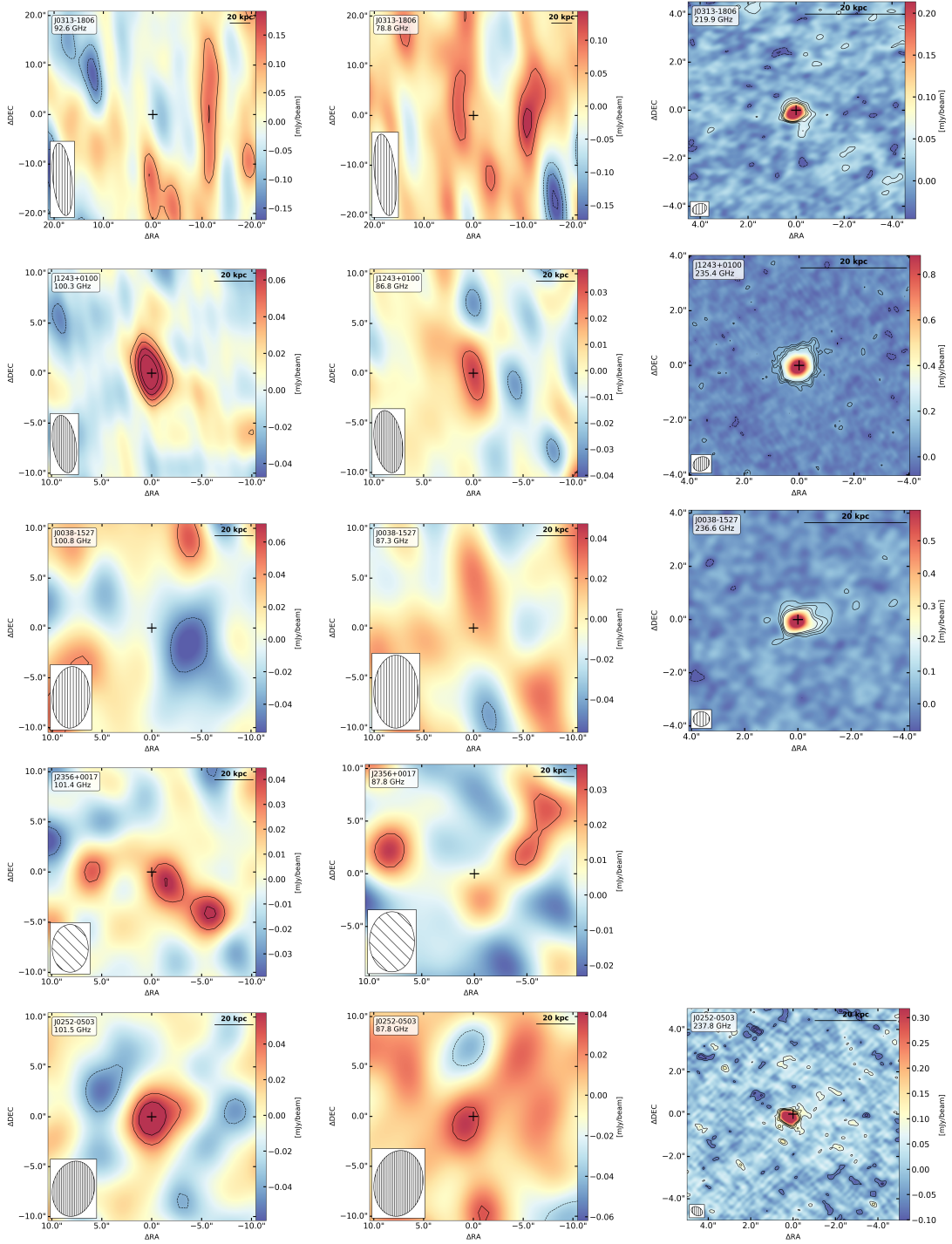


Fig. B.1: Continuum maps. The source name and the observed frequency are in the upper-left corner. The optical position of the quasar is reported with a black cross. Contour levels are -3 , -2 , 2 , 3 , 4 , 5 σ significance, where the RMS is listed in Table 1. The clean beam for each observation is shown in the lower-left corner of the diagram, and the corresponding size is reported in Table 1.

Appendix C: Comparison sample of high- z quasars

In Table C.1, we report the information collected from the literature for 21 quasars at redshift $z \gtrsim 6$ and a quasar at $z \sim 5$. Quasars have been selected to have observations of CO emission lines, and properties derived from the far-IR SED fitting. In addition, 19 out of the 21 quasars at $z \gtrsim 6$ have $L_{\text{[CII]}}$ measurement. We report $L'_{\text{CO}(1-0)}$ derived from $L'_{\text{CO}(J+1--J)}$ available in the literature (see column J_{up}), assuming for all objects the same fixed CO-SLED that we used in section 3. In particular, we assumed $r_{J+1,J} = L'_{\text{CO}(J+1--J)}/L'_{\text{CO}(1-0)}$ as follows: $r_{7,6} = 0.65$, $r_{6,5} = 0.9$, $r_{2,1} = 1$. The host galaxy SFR is then derived from L_{FIR} by adopting a Chabrier IMF. Moreover, we report only the measurement uncertainties for the sources for which these quantities were

reported in the literature (see references). During calculations and fitting procedures described in section 3, for each measurement without uncertainty, we assign an error that is equal to the median of the relative uncertainties available.

Source	RA DEC	z	$\log(L_{bol})$ [erg/s]	$\log(M_{BH})$ [M_{\odot}]	(L_{CII}) $10^9 L_{\odot}$	$\log(L_{TIR})$ [L_{\odot}]	$(L'_{CO(1-0)})$ $10^{10} \text{ K km/s pc}^2$	$\log(M_{dust})$ [M_{\odot}]	Ref
	J2000								
SDSSJ0100+2802	01:00:13.02 +28:02:25.80	6.3258	48.187 ± 0.001	10.29 ± 0.01	3.56 ± 0.49	12.42 ± 0.09	3.54 ± 0.46	7.36 ± 0.13	[1,8,13]
J010953.13-304726.30	01:09:53.13 -30:47:26.32	6.7909	46.71 ± 0.05	9.12 ± 0.16	2.4 ± 0.2	12.08 ± 0.09	11.54 ± 2	8.48 ± 0.4	[2,9,15]
VDESJ0224-4711	02:24:26.54 -47:11:29.40	6.522	47.53 ± 0.03	9.11 ± 0.06	5.43 ± 0.15	13.52 ± 0.2	1.48 ± 0.22	7.97 ± 0.11	[3,10]
PSOJ036.5+03	02:26:01.87 +03:02:59.24	6.541	47.3 ± 0.09	9.48 ± 0.12	5.8 ± 0.7	12.71 ± 0.11	1.65 ± 0.18	7.79 ± 0.15	[2,8,16]
J0305-3150	03:05:16.92 -31:50:55.90	6.6145	46.88 ± 0.13	8.95 ± 0.14	3.9 ± 0.2	12.83 ± 0.013	3.08 ± 0.46	8.95 ± 0.25	[2,9,16]
SDSS J0338+0021	03:38:29.31 +00:21:56.30	5.0278	47.25	9.4 ± 0.12	5.69 ± 0.83	13.08	1.12 ± 0.17	8.33 ± 0.03	[4,11]
J0840+5624	08:40:35.09 +56:24:19.90	5.8441	46.713 ± 0.002	9.55 ± 0.19			1.81 ± 0.64 ^a		[5,12]
J0927+2001	09:27:21.82 +20:01:23.70	5.7716	46.99 ± 0.003	9.69 ± 0.12			4.75 ± 1.15 ^b		[5,12]
PSO J159.2257-02.5438	10:36:54.19 -02:32:37.94	6.3822	47.26 ± 0.008	9.68 ± 0.05	1.19 ± 0.07	12.2	1.05 ± 2	7.89 ± 0.04	[1,11]
VIK J1048-0109	10:48:19.09 -01:09:40.29	6.6766	47.023 ± 0.012	9.53 ± 0.11	2.77 ± 0.08	12.89	1.72 ± 0.17	8.7 ± 0.11	[1,11]
DELS J1104+2134	11:04:21.58 +21:34:28.85	6.7672	47.18 ± 0.03	9.23 ± 0.04	1.82 ± 0.28	12.7	1.18 ± 0.23	8.53 ± 0.18	[6,11]
SDSSJ1148+5251	11:48:16.10 +52:51:50.00	6.4189	47.538 ± 0.002	9.94 ± 0.02	4.2 ± 0.35	13 ± 0.06	3.2 ± 0.3 ^b	8.51 ± 0.1	[5,10,17]
PSOJ183+05	12:12:26.98 +05:05:33.49	6.4386	47.351 ± 0.006	9.67 ± 0.06	25.3 ± 0.4	13.08 ± 0.15	3.51 ± 0.39	8.65 ± 0.08	[1,13,10]
ULASJ1319+0950	13:19:11.29 +09:50:51.40	6.1336	47.247 ± 0.001	9.46 ± 0.03	4.4 ± 0.9	12.99 ± 0.008	1.8 ± 0.23	8.8 ± 0.16	[1,8,10]
PSO231-20	15:26:37.84 -20:50:00.66	6.5864	47.28 ± 0.09	9.48 ± 0.19	2.87 ± 0.15	13.28 ± 0.09	2.15 ± 0.2	8.72 ± 0.04	[2,14,10]
PI308-21	20:32:10.00 -21:14:02.40	6.2354	47.34 ± 0.004	9.41 ± 0.07	1.73 ± 0.14	12.42 ± 0.18	<0.29	7.7 ± 0.2	[1,14,11]
J2054-0005	20:54:06.49 -00:05:14.80	6.0397	47.092 ± 0.013	9.34 ± 0.05	3.3 ± 0.5	12.73 ± 0.007	0.86 ± 0.31	8.03 ± 0.09	[1,8,11]
VIMOS2911001793	22:19:17.22 +01:02:48.90	6.1503	47 ± 0.07	9.49 ± 0.05	2.59 ± 0.13	12.24 ± 0.03	1.42 ± 0.22	7.92 ± 0.04	[7,8,11]
PSO J338.2298+29.5089	22:32:55.15 +29:30:32.23	6.6668	47.61 ± 0.16	9.43 ± 0.15	2 ± 0.1	12.31 ± 0.11	0.94 ± 0.23	7.96 ± 0.05	[2,8,11]
SDSSJ2310+1855	23:10:38.89 +18:55:19.70	6.0028	47.5 ± 0.001	9.86 ± 0.06	8.7 ± 1.4	13.2 ± 0.004	0 ± 0	8.64 ± 0.06	[5,8,18]
J2348-3054	23:48:33.35 -30:54:10.28	6.9018	46.63 ± 0.17	9.3 ± 0.15	1.9 ± 0.3	12.63 ± 0.03	12.46 ± 2.62	8.04 ± 0.12	[2,9,16]
PSOJ359-06	23:56:32.45 -06:22:59.26	6.1726	47.409 ± 0.005	9.58 ± 0.09	2.42 ± 0.15	12.32	0.89 ± 0.25 ^b	7.97 ± 0.04	[1,11]

Table C.1: Quasar properties. From left to right, columns include source name, coordinates, redshift, logarithm of bolometric luminosity, logarithm of the BH mass, [CII] luminosity, logarithm of the total infrared luminosity, CO(1-0) luminosity, upper J of the CO transition considered, logarithm of the dust mass. CO(1-0) luminosities are derived by assuming a CO-SLED from CO(7-6) emission line, apart from ^a and ^b, where we used CO(2-1) and (6-5) transitions. References for optical and far-IR measurements are: [1] Shen et al. (2011); [2] Mazzucchelli et al. (2017); [3] Wang et al. (2021); [4] Dietrich & Hamann (2004); [5] Shen et al. (2019); [6] Yang et al. (2021); [7] Kashikawa et al. (2015); [8] Decarli et al. (2018); [9] Venemans et al. (2017c); [10] Tripodi et al. (2024a); [11] Decarli et al. (2022); [12] Wang et al. (2011); [13] Decarli et al. (2023); [14] Pensabene et al. (2022); [15] Venemans et al. (2017b); [16] Kaasinen et al. (2024); [17] Stefan et al. (2015); [18] Feruglio et al. (2018).